Exploring Colloidal Quantum Shells as a Novel Lasing Medium on an Integrated Silicon Nitride Platform

Ivo Tanghe,[*,†,‡,¶] Korneel Molkens,[†,‡,¶] Tom Vandekerckhove,[†] Amelia Waters,[§] Jacob Beavon,[§] Dries van Thourhout,[†] Mikhail Zamkov,[‖,§] and Pieter Geiregat[‡,¶]

†*Photonics Research Group, Ghent University, Belgium*

‡*Physics and Chemistry of Nanostructures, Ghent University, Belgium*

¶*NoLIMITS Center for Non-Linear Microscopy and Spectroscopy, Ghent University, Belgium*

§*Department of Physics, Bowling Green State University, Bowling Green, Ohio*

‖*The Center for Photochemical Sciences, Bowling Green State University, United States*

E-mail: ivo.tanghe@ugent.be

Abstract

In recent decades, the field of photonics has witnessed remarkable advancements in the development of novel laser materials that span a diverse range of applications, from telecommunications to medical devices. This paper delves into an exploration involving the utilization of colloidal "Quantum Shells" as an innovative platform for laser development. We present a comprehensive investigation, encompassing both fundamental characterization and advanced applications, with the overarching goal of establishing the viability of these intriguing materials as efficient lasing mediums.

Introduction

Ever since the groundbreaking discovery of optical gain in CdSe-based Colloidal Nanocrystals in the year 2000,[1] the pursuit of more efficient solution-processable gain materials has resulted in the development of a vast library encompassing a diverse range of atomic structures, elemental compositions, and geometric configurations. Through deliberate modifications to the system, achieved either by incorporating semiconductor shell(s) to enhance charge separation from the surface,[2,3] or by changing the geometry to fundamentally reshape the underlying physical mechanism for optical gain,[4] fundamentally better materials for various applications are now available. This can be seen in working opto-electronic devices with room-temperature continuously operated Amplified Spontaneous Emission (ASE) on integrated devices;[5] near-zero threshold optical gain[6,7] and ASE;[8] and LEDs performing at better than industry standards.[9] High excitation applications specifically, like lasers and ASE-based devices, add additional complexities. Inorganic systems hold promise over other solution-processible materials like organic dyes, due to their stability under these high excitation conditions.

Exploring the criteria that make a solution-processable material valuable in a non-linear optical device remains a topic of ongoing discussion within the community. We can categorize these materials based on three non-linear optical material parameters: the inverted-sate (or "gain"-) lifetime τ_G, the threshold carrier density n_{th} and the material gain coefficient g_i. These are reported for a variety of materials in the library, where for each metric there are superior materials: type II Quantum Dots (QDs)[10–13] and electron-doped systems,[6] with record low n_{th} but limited g_i; 2D nanoplatelets,[4,14–16] with record g_i but sub-nanosecond τ_G; and the family of core/shell CdSe/CdS-based QDs which offer a compromise solution on the three fronts, driven mainly by small bi-exciton redshifts of less than 10 meV.[2] The latter, which has been the most studied, is the most advanced in terms non-linear devices. While these results are impressive, instead of having a material that combines good values for each metric, a compromise between them must be made, as there is an intrinsic interplay between

specifically g_i and τ_G for QDs. Larger nanocrystals with a small core typically showcase long lifetimes, but the price for that is a lower material gain. Opting for extended gain lifetimes over material gain preferences constrains the potential power output. An interesting observation that can be made is that in recent years, there has been more and more interest into nanocrystals with larger and larger active volumes specifically. For CdSe/CdS core/shell QDs, it has been observed that large cores provide the best gain metrics.[2] Colloidal Quantum Wells also boast with record high material gain values.[4] Recently, work has been published showing that going beyond the bohr diameter and using so-called "bulk nanocrystals" shows impressive gain metrics, specifically for the material gain, in combination with multiple nanoseconds gain lifetimes.[17]

Here, we expand upon one novel material platform in the library, the CdSe/CdS Quantum Shell (QS).[13,18] This material consists of multiple shells, where contrary to typical QDs, the material possessing the smallest band gap (CdSe) is located not within the core, but rather in the initial shell. The core and the other shell consist of a material with a larger band gap (CdS), and the whole structure is encapsulated with a ZnS shell for surface passivation. QSs have previously been reported to have very long gain lifetimes of up to 6 ns.[13] we confirm these results, and furthermore show that the gain magnitude can reach impressive values, with a comparable to state-of-the-art threshold note: add more values here when new TA is done. These findings highlight a promising material candidate for lasing applications. To validate these results, lasing is demonstrated on an integrated Silicon Nitride (SiNx) on Silicon Oxide (SiOx) platform. This platform is specifically tailored for visible low-loss applications.[19] A Photonic Crystal (PhC)-type cavity is used,[20,21] similar to previous demonstrations of solution-processible based materials.[22,23] Here, holes are etched periodically in the SiNx, and is then overcoated with the QSs through spincoating. A difference compared to other work on PhC cavities is the low index contrast in these devices. Often bonding is used to connect a chip containing a gain material and a chip containing the cavity, leading to an interface between air ($n = 1$) and a semiconductor ($n = 3.8$).[24]

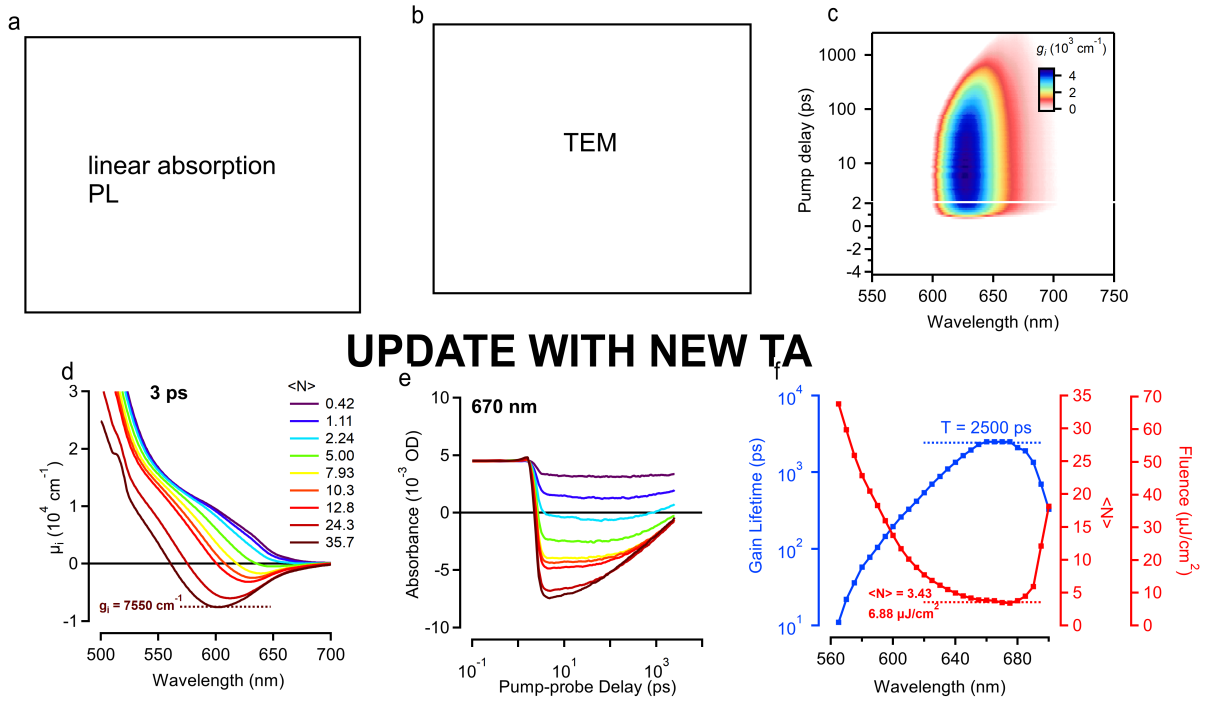

Figure 1: Linear Characteristion and Transient Absorption data. Complete with new TA dataset

Here, however, the contrast is between SiNx ($n = 2$) and the QSs ($n = 1.7$). The cavity is designed such that surface emission occurs. As a first demonstration, lasing action is shown over a wide spectral region (580-660 nm), with comparable thresholds in literature on solution-processible materials. These go from 175 to 15.9 µJ/cm^2 for femtosecond excitation and 462 - 67 kW/cm^2 for quasi-CW operation. The lowest thresholds are reached for devices that operate closest to the bandgap of the QSs (640-660 nm). Finally, the lasing operation is studied more in-depth and theoretically explored by looking into the low excitation PL spectra of the grating, combined with FDTD simulations performed in Lumerical to find theoretical resonances. Through polarisation measurements, specific lasing modes of the cavities can be identified.

Transient Absorption Spectroscopy

The sample used emits around 665 nm (Figure 1a). A Quantum Yield of close to 100% is measured. It consists of a 8.5 nm CdS core, followed by a 1.9 nm CdSe shell. This system emits at 653 nm. After additional CdS/ZnS shelling, the total particles are 21-22 nm, consisting mainly of CdS and we estimate around a 1 nm thick ZnS shell, found through a TEM analysis (Figure 1b). This additional shelling causes a redshift of the PL to get to the displayed PL. The sample used here is very similar to the one used in the work of Harankahage *et al.*[18]

We studied the optical gain by means of femtosecond TA. A 110 fs pulse is used to excite a QS dispersion to create electron-hole pairs. We use off-resonant excitation at 515 nm (2.4 eV) to create hot carriers in the system. After the initial pump pulse, a second short but broadband probe pulse is injected into the sample. By measuring the difference in transmission when the QS sample is excited or not, a change in absorption ΔA can be measured for a broad wavelength range. By then in succession changing the delay between the pump and the probe, this change in absorption can be measured as a function of time. By adding the linear absorption A_0 to the measured ΔA, and checking where this signal becomes negative, a gain map can be created as shown in Figure 1c. This map shows for what wavelengths there is optical gain, how strong it is, and how long the optical gain persists in this system. By varying the excitation power, multiple of these maps can be measured to find the gain threshold.

In Figure 1d, the absorption spectrum is shown for a 3 ps pump-probe delay for multiple excitation densities, showing a gain window stretching from 550 to 680 nm at high powers. Interestingly, there does not seem to be any sort of saturation of the gain.. In Figure 1e, the absorption is shown at 670 nm, near the band gap, from which the gain lifetime can be found. Here, we see.... Finally, in Figure 1f, the found gain lifetime (blue), and the threshold (red) are plotted together, showing the inversely proportional relationship between these two parameters. This shows....

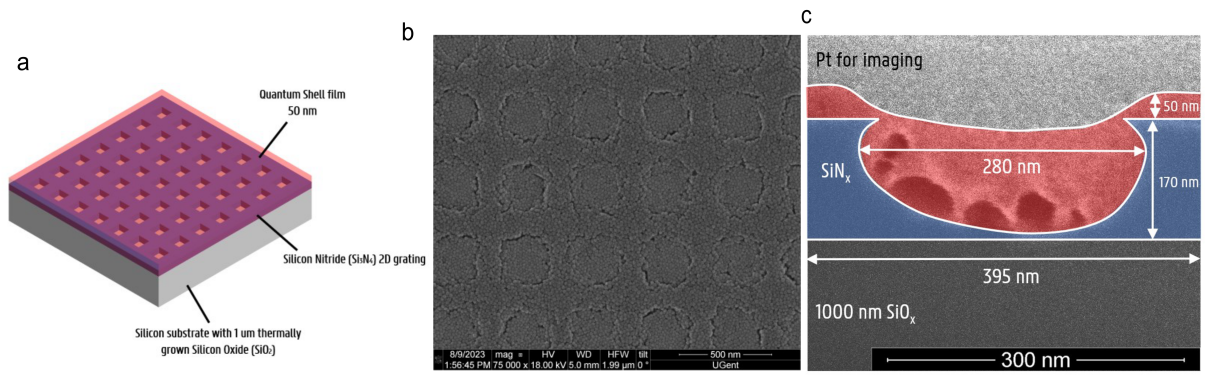

Figure 2: Schematic of the used Photonic Crystal Cavities. (a) A schematic of the device. (b) SEM top view of a device, with a period of 385 nm. The QS film is thinner locally where the holes in the SiNx film are. (c) A cross-section of the same device, also taken with SEM. The thinning of the QS film is also visible here. Rough sidewalls of the SiNx etch and a nearly full etch can be observed. The voids observed in the QS film within the holes are a consequence of the ion beam etching process, which selectively removes the QSs.

Ultimately, the QSs show an impressive combination of strong material gain, with record long gain lifetimes, outcompeting both colloidal QDs (both in gain magnitude and gain lifetime) and QWs (in gain lifetime).

Photonic Crystal Cavities

The resonating wavelength within a cavity follows Bragg's Law, expressed by the equation:

$$m \cdot \lambda_{Bragg} = 2 n_{eff} \Lambda \tag{1}$$

Here, m denotes the order of diffraction, λ_{Bragg} is the resonant wavelength, n_{eff} is the effective refractive index in the structure, and Λ is the period of the grating. A second order grating was used to achieve surface emission. In this study, gratings were designed with a square lattice, featuring periods spanning from 320 to 460 nm at 5 nm intervals. This range was determined based on an estimate of the effective index, ensuring a comprehensive scope.

Laterally, the devices are 600 × 600 periods, varying from 192 × 192 µm to 276 × 276 µm. A schematic of a device is shown in Figure 2a. The devices are designed with a duty

cycle of 60%, defined as the ratio between the side of the hole and the total period. SEM images in Figure 2b,c show a device with a period of 395 nm. The top view shows that the different QSs can be clearly resolved despite the oxide cladding. The presence of holes results in localized thinning of the spin-coated film of QSs in those specific areas. From the cross-section it can furthermore be seen that the sidewalls are very rough, and that the SiNx is nearly etched fully through. Moreover, a duty cycle of around 70% is found, indicating an overexposure or overetching is occuring as they are designed with a duty cycle of 60%. The duty cycle is defined as the length of a side of the hole divided by the period.

Lasing through Photonic Crystal Surface Emitting Devices

First, the devices were measured using the same 110 fs pulsed excitation at 515 nm consistent with the TA measurements. An example of a measurement where the excitation power is changed is illustrated in Figure 3a (top), for a period of 385 nm, showing lasing at 637.5 nm. The inset graph depicts peak counts as a function of fluency, revealing distinct threshold behaviour, with a measured threshold of 35.8 µJ/cm^2. Figure 3b (top) provides a closer view of the lasing peak, revealing an additional peak emerging at higher fluencies. Devices exhibited lasing across periods ranging from 335 nm to 405 nm, corresponding to resonant wavelengths spanning 580 to 660 nm. Figure 3c displays the normalized lasing peaks for all devices, where on top the link between period and resonance is made. Transitioning from 380 to 385 nm results in a shift back to shorter wavelengths. We will come back to this jump in the next section. Figure 3d illustrates device thresholds in red, revealing the lowest threshold within the range of 640-660 nm, measured at 15.9 µJ/cm^2.

Subsequently, the identical devices underwent excitation employing a 7 ns pulsed laser at 532 nm. Given that the pulse duration exceeds the gain lifetime, this excitation scenario involves the creation and annihilation of electron-hole pairs to generate photons multiple

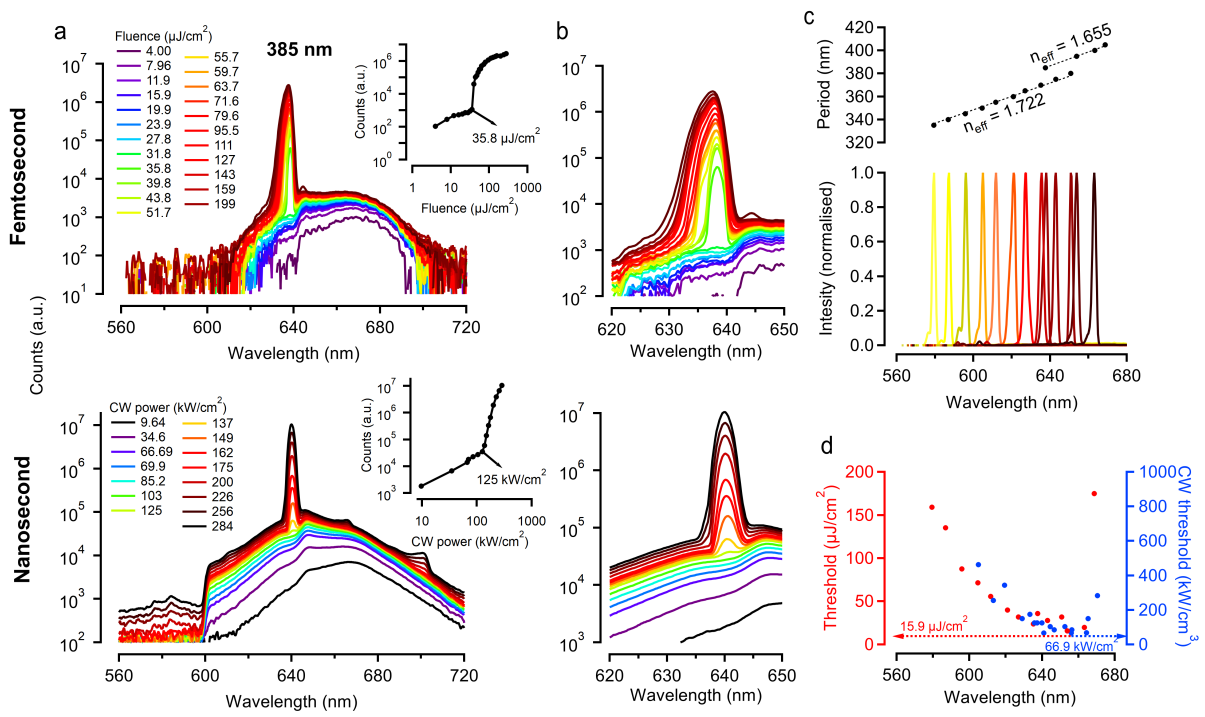

Figure 3: Observed lasing in PhC cavities with QSs as a gain material. (a) Spectra under various excitation strengths for the device with a period of 385 nm, for femtosecond excitation (top) and quasi-CW excitation (bottom). The insets show the peak counts for all excitation strengths. (b) Zoomed in spectra around the peak for femtosecond excitation (top) and quasi-CW excitation (bottom). (c) All normalised lasing peaks with their corresponding period. A distinct jump is observed going from 380 to 385 nm. (d) Femtosecond (red) and quasi-CW (blue) thresholds for all devices, showing clear correlation and minima between 640-660 nm.

times within a single excitation pulse. From an optical perspective, the process results in the formation of a stable mode, termed quasi-Continuous Wave (quasi-CW) excitation. Spectra from exciting in this manner is shown in Figure 3a (bottom). Here, the power density is portrayed as a CW equivalent power rather than fluency. This representation reflects the optical power the pump would exert if the excitation source were continuously active. Once again, lasing is observed, characterized by a distinct threshold behavior at 125 kW/cm^2. Examining the magnified peak in Figure 3b (bottom) reveals a more symmetrical mode when compared to the femtosecond excitation. This can be explained by the difference in excitation. With quasi-CW excitation, the extended duration of population inversion leads to mode competition, resulting in the coupling of gain to a specific mode. In contrast,

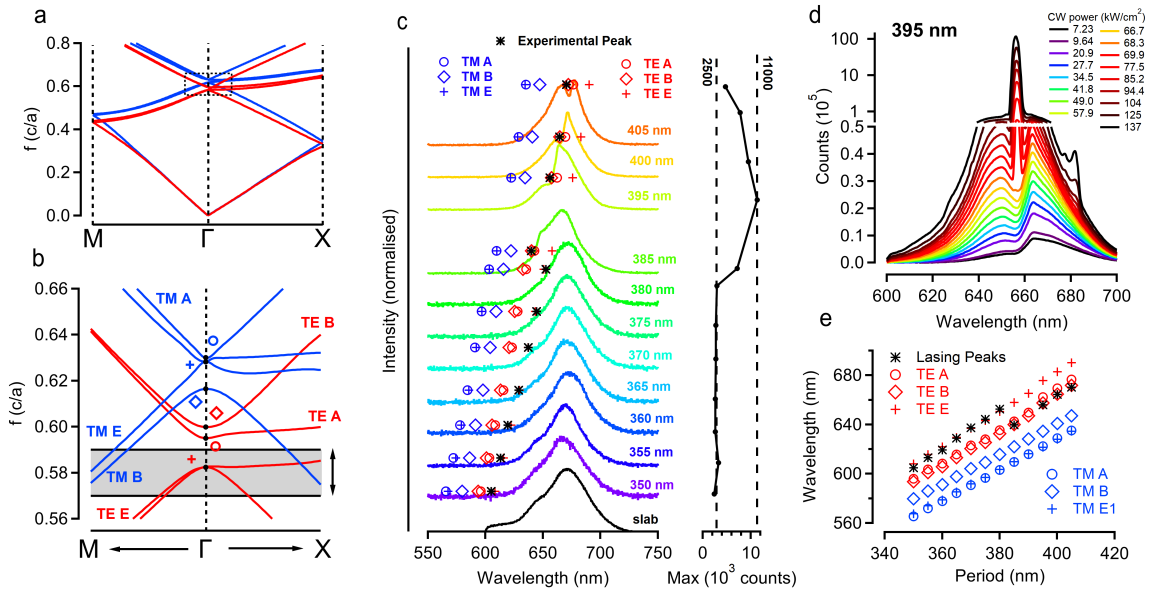

Figure 4: Photonic Banddiagram simulation and comparison to measured spectra. (a) Bandstructure going from M to Γ to X. (b) Zoom in around Γ, with specifically assigned modes. The displayed bands are shown in (a) with the black box. (c) PL spectra for various periods (colored curves) with measured lasing wavelength (black diamonds) and simulated modes for all six bands (red and blue markers). The curve on the right shows the maximum counts measured for each device. (d) Simulated (red and blue markers) and experimental lasing peak (black diamonds) as a function of period, showing excellent agreement. (e) Spectra under various excitation strengths at 395 nm, particularly focused on the PL. Here, the dip is clearly visible.

femtosecond excitation generates a population that lacks sufficient time to establish a stable mode before the reversal of population inversion occurs. These quasi-CW thresholds are also depicted in Figure 3d, represented in blue. With the exception of some shorter period devices (335-345 nm), all devices exhibit quasi-CW lasing. The lowest observed threshold is 66.9 kW/cm^2.

Understanding Lasing with Photonic Crystal Cavities

To comprehend the lasing mechanism and resonance behavior of optical modes in these devices, we conducted simulations of the photonic bandstructure through FDTD simulations. Further details on these simulations are outlined in Supporting Information X. By exciting

all optical modes for a specific in-plane wavevector $\vec{k}_{||}$, we can identify resonances at distinct frequencies. Subsequently, sweeping the values of $\vec{k}_{||}$ reveals the photonic bands. Our approach involved traversing from the M-point $(\frac{\pi}{a}, \frac{\pi}{a})$ to the Γ-point (0,0), and subsequently to the X-point $(\frac{\pi}{a}, 0)$ — a convention commonly followed in the literature.[25,26] Figure 4a illustrates these findings, specifically for a period of 385 nm. Given our focus on surface-emitting lasers, our primary interest lies in the Γ-point. At this point, $\vec{k}_{||}$ equals zero, allowing only upward scattering, or redirected in-plane. In Figure 4b, a bandstructure with a more limited range of $k_{||}$-values is presented, covering only 20% of the distance to the X-point and M-point.

Figure 4b reveals a total of eight bands; however, at the Γ-point, these reduce to six, with two pairs of modes (E_1 and E_2) becoming degenerate. Four of these bands correspond to TE bands (primarily featuring electrical fields in-plane), while the remaining four represent TM bands (mainly characterized by magnetic fields in-plane). These are technically quasi-TE and quasi-TM due to minimal symmetry breaking out of plane caused by the SiOx substrate. The bands can be assigned to TE or TM by looking at the fields in the cavity, See Supporting Information X. In literature, Photonic Crystal based lasers frequently focus on TE bands, given the use of Quantum Wells as gain material.[25,26] Due to the specific stacking of the Quantum Wells, optical gain does not couple to TM modes. Here, the spherical symmetry of the particles necessitates consideration of both TE and TM modes. The designations (A, B, and E) specifically correspond to the symmetry of the in-plane fields. A and B modes exhibit anti-symmetrical electric fields for TE (magnetic fields for TM) concerning the in-plane axis, whereas E modes feature symmetrical electric fields for TE (magnetic fields for TM). The anti-symmetry induces destructive interference for upward scattering light, essentially rendering it forbidden. Consequently, for A/B-modes, light is effectively confined within the Photonic Crystal, resulting in an infinite Q-factor for an infinite number of periods. In a realistic device, the Q-factor will drop since this perfect anti-symmetry is broken near the edge. For the E-modes, however, the situation differs, leading to significantly

lower Q-factors for the cavity even for an infinite structure.

Increasing the period causes the entire bandstructure to shift downward in frequency or to longer wavelengths. In relative terms, this shift corresponds to the gain band moving upwards in the band diagram, as illustrated in Figure 4b by the grey band. Therefore, by selectively exciting the six modes at the Γ-point separately for various periods, an attempt can be made to align them with the experimentally measured lasing peaks, as explained in more detail in Supporting Information X.

For deeper insights, the impact of the PhC on the PL trace can be examined, as illustrated in Figure 4c. These curves are found by exciting the devices with powers less than the threshold. It can be observed that with an increase in the period, the PL trace undergoes alterations compared to the PL from the slab (depicted in black at the bottom of the Figure). This suggests a nuanced interplay between the PL from the QSs and the emission direction permitted by the cavity. Especially for periods of 385 nm and beyond, distinctive additional features become evident on the traces: a two-peak pattern with a noticeable dip in between. This dip is attributed to the overlap between the positions of the TE A and B bands at the Γ-point and the PL spectrum, as outcoupling the PL at this point is forbidden. Additionally, there is a noticeable increase in counts for these specific devices. The PL curves shown in Figure 4c are normalised, and their maximum is displayed on the right. Shorter period devices peak around 2500 counts, while longer period devices reach nearly 5 times higher, hitting 11000 counts. For these periods specifically, the PL of the QSs overlaps with numerous photonic bands, resulting in a high Density Of States (DOS) near the Γ-point. This directs much of the PL upwards. The combination of the anti-symmetrical electrical field for the A/B modes, leading to the local dip in the PL, along with the enhancement of the PL around this dip due to a high DOS, aligns well with the experimental data. For instance, Figure 4d presents spectra for different excitation powers, with a focused view on the PL at the bottom half of the graph. Notably, the distinct dip in the PL aligns precisely with the position of the lasing, reinforcing the notion that this corresponds to the TE A or B mode.

Turning focus now to the lasing peaks, simulations for the six resonant modes across different periods are illustrated as circles (A), diamonds (B), and crosses (E) in red (TE) and blue (TM), juxtaposed with the measured lasing peaks represented by black asterisks. Excellent alignment is observed between simulation and experiment. Devices in the range of 350-380 nm coincide with the TE E mode, while those in the 385-405 nm range align with the TE A or B mode. This alignment is depicted in Figure 4e.

Despite the theoretical possibility of TM lasing in this scenario, no such observation was made. This is attributed to the out-of-plane nature of the electric fields for TM modes, coupled with the pronounced roughness of the surface (as evident in Figure 2b), resulting in increased scattering compared to TE modes. Alternatively, better overlap between the gain band and the TM modes could be achieved by shifting to even larger periods than those used in the current chip.

To support our hypothesis, we examine the far field of the devices. Specifically for the A/B modes, it is well known that the far field of a device with symmetrical shapes in a unit cell will manifest a ring shape.[17,27] Conversely, for the E mode, it assumes the form of a Gaussian. The emission angle is determined by both the refractive index contrast and the number of periods. This characteristic ring shape is the same for both the TE and TM modes, although their polarization differs: the TE far fields have azimuthal polarisation, while for TM, it is radial. Subsequently, by introducing a polarizer into the experimental setup, it becomes possible to discern whether the observed ring in the far field is the result of TE or TM modes. Figure 5a (top) illustrates a simulated far field, breaking down its components in the x and y directions. This is then compared with the experimental measurement shown in the bottom panel, for a device with a period of 395 nm, although the far field is similar for all devices with periods 385 - 405 nm. The unmistakable ring shape is clearly visible in the far field. When we apply horizontal polarization, distinct vertical lobes emerge, and vice versa. This observation serves to confirm the TE nature of the mode.

Apart from the prominent ring shape, a distinctive cross shape emerges, featuring inter-

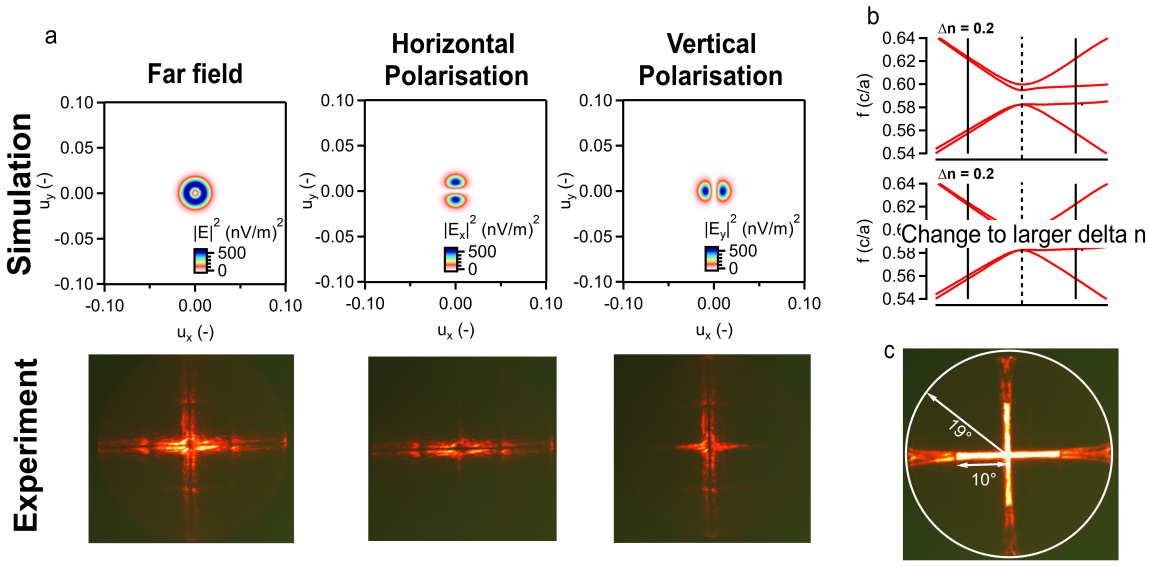

Figure 5: Far fields of devices. (a) Far fields with and without a polariser. (top) Far fields shown in a simulation. (bottom) Measured far field for the device with a period of 395 nm. (b) Measured far field of the device with a period of 360 nm. (b) TE modes around the Γ-point for our device, where $\Delta n = 0.3$ (top), compared to a hypothetical $\Delta n = 1.2$ device with the same period. (c) Far field pattern measured for a device with a period of 360 nm, where the lasing corresponds to the TE E mode.

secting lines with a discernible split. Prior research has illustrated a cross-shaped far field,[28] where, post-threshold, the laser initially exhibits a Gaussian-shaped far field, transitioning to a cross shape at higher powers. Notably, in our case, the cross shape materializes immediately after threshold, and a splitting is observed in the arms of the cross. We attribute the former phenomenon to the low index contrast in our system, resulting in flat bands during the transition from the Γ-point to the X-point for specific bands. This characteristic facilitates easy coupling of light to modes with a non-zero $k_{||}$, as there is only a very small energy difference, allowing it to be emitted at a specific angle. To illustrate this, Figure 5b compares the bandstructure from our system to a theoretical one with a higher index contrast of $\Delta n = 1.2$. Besides an inevitable frequency shift, it is clear that the dispersion relation in this system becomes much steeper. Consequently, a lasing peak with a FWHM of about 2 nm, as we observe, will have a much larger angular spread in our system compared to this hypothetical, large index contrast one. Regarding the observed splitting, we propose that

as light leaks out of the mode, it subsequently scatters off-resonantly on the 1D gratings in the x and y directions, leading to a cross with a splitting. In the case of the E-mode, where scattering is resonant on the 1D grating, no such splitting occurs, as depicted in Figure 5c. The resulting cross emission cone maintains an angle of about 10°. All devices with periods from 335 to 380 nm exhibit this cross shape.

Conclusions

In this study we investigated the optical gain in Colloidal Quantum Shells and used them in integrated devices. Our findings not only confirm the long gain lifetimes previously observed,[13] but also unveil their high material gain, surpassing benchmarks set by colloidal Quantum Dots.[5,29] To demonstrate their validity, the QSs are used as a gain material on an integrated SiNx/SiOx based platform, with a cavity based on a Photonic Crystal design. Lasing is achieved with both femtosecond and quasi Continuous Wave operation, showcasing competitive thresholds (16 µJ/cm^2 for femtosecond and 67 kW/cm^2 for quasi-CW) in comparison to reported devices in the literature.[22] We furthermore explored the theoretical background of operation of these devices. By aligning our observed modes with those predicted through simulations, we provide a comprehensive theoretical foundation. This exciting first look into utilizing colloidal QSs in integrated devices not only highlights their potential but also positions them as promising candidates for more intricate and practical applications.

Methods

Materials Synthesis to do

Transient Absorption Spectroscopy Samples were excited using 110 femtosecond pump pulses at 515 nm, through second harmonic generation in alpha-BBO. Probe pulses were generated in a 1 mm thick CaF_2 crystal using the 1030 nm fundamental. The pulses were delayed relative to the pump using a delay stage with maximum delay of 3 ns for 515 nm pumping. The probe spectrum in our experiments covers the UV-VIS window from 420 nm up to 700 nm. The quantum shells were dispersed in an optically transparent solvent (toluene) and continuously stirred to avoid charging or photo-degradation. The pump wavelength and sample concentration were chosen to obtain an optimal trade-off between having a good signal at the band-edge transitions, while still not having a too strong absorption at the pump-wavelength as to assure a uniform pumping of the sample.

The average number of absorbed photons (or equivalently created excitons) at time zero, noted as $\langle N \rangle$, can be calculated from the photon flux J_{ph}, the cuvette length L and the nanocrystal absorption cross section at the pump wavelength σ_{λ_p}: $\langle N \rangle = J_{ph} \times \sigma_{\lambda_p} \times \frac{1-e^{-\alpha_{0,\lambda_p} L}}{\alpha_{0,\lambda_p} L}$. The photon flux is calculated from the beam area, obtained through a Thorlabs CCD beam profiler, and defined as $A_{beam} = 2\pi \times \sigma_x \sigma_y$ where σ_i is the standard deviation in the $i = x, y$ direction. Note that the carrier density n follows as $\langle N \rangle / V$, with V the volume of the nanocrystal.

Femtosecond Photoluminescence Spectroscopy (PROBABLY NOT NEEDED) For the detection of the broadband PL transients on a sub-picosecond timescale, we used the transient grating PL technique.[30] The output of a femtosecond Ti:S laser was split into pump and gate parts. For the pump part, second harmonic (400 nm) generation was used in the experiments and focused to a 50 μm^2 spot onto the sample. During the measurement, the sample was continuously stirred in a 1 mm cuvette to avoid photo-induced degradation

effects or charging of the nanoparticles. The PL signal from the sample was collected and refocused onto the gate medium, a 1 mm fused silica crystal, using a pair of off-axis parabolic mirrors. For the gate part, about 40 μJ of the 800 nm output was split using a 50/50 beam splitter to generate the two gate beams and focused onto the gate medium at a crossing angle of approximately 8 degrees and overlapped with the PL in a boxcar geometry. The two gate beams, which spatial and temporal overlap inside the gate medium, generate a laser-induced grating. This transient grating acts like an ultrafast optical shutter to temporally resolve the broadband PL signals by diffracting the gated signal from the PL background. Two achromatic lenses collimated and focussed the gated signals onto the spectrometer entrance (Princeton Instruments SP 2150), and the gated PL spectra were measured by an intensified CCD camera (Princeton Instruments, PIMAX3). The time delay between pump and gate beams was controlled via a motorized optical delay line. For each transient PL spectrum, 120 000 shots at each gate time delay were accumulated.

Cavity Fabrication Silicon substrates covered with 1 µm thermally evaporated silicon oxide are used as the starting chip. These are first cleaned using acetone and isopropanol, followed by an oxygen plasma treatment. By Plasma-Enhanced-Chemical-Vapour-Deposition, 180 nm of silicon nitride is deposited at 270 °C. To create the grating, electron beam lithography is used. First, the positive resist AR-P 6200.13 is used, spincoated at 4000 rpm, to achieve resist thicknesses of 400 nm. The chip is then baked at 150 °C for 60 seconds. After this, AR-PC 5090 is spun as a protective coating, also at 4000 rpm to achieve a layer around 40 nm thick. This conductive coating increases electron beam lithography resolution. After spincoating, the chip is baked at 90 °C for 120 seconds. E-beam lithography is done using a Raith Voyager system, using a dose of 160 µC/cm^2. After exposure, the chip is developed by putting it into a bath of n-amyl-acetate for 60 seconds, following an isopropanol bath for 60 seconds. A specifically optimized reactive ion etching (RIE) process based on a CF_4 / H_2 chemistry is used to etch the silicon nitride layer, and is almost etched completely through.

After the etch, the remaining resist is cleaned off using an oxygen plasma treatment. Finally, the Quantum Shells are spincoated on top of the chip, with a film thickness of about 50 nm.

Laser Measurements For femtosecond excitation, the same 515 nm laser as above is used, with 110 fs pulses. The beam is reflected on a dichroic mirror with a cutoff wavelength of 600 nm, and is then focussed perpendicular on the sample. The surface emission gets transmitted through the dichroic. Following this, a 50/50 splitter is used, where 50% of the light is focused on a fiber for spectral analysis, and 50% is focused on a camera for imaging. The fiber goes to a Andor Shamrock 750 Spectrograph.

The nanosecond excitation uses the same optical setup, but a Ekspla NL202 laser is used, with a fundamental at 1064 nm, and second harmonic generation through alpha-BBO doubles this to 532 nm. The pulse duration is 7 nanoseconds. Here, the signal is measured using an Andor Kymera 328i.

Photonic Crystal Simulations In supporting information?

Sections on: (1) how the simulation is set up. (2) How the bandstructure is determined. (3) How TE or TM is assigned. (4) How specific modes are excited. (5) How the far field is found. (6) How to extract E_x and E_y.

Supporting Information

The Supporting Information provides ...

Acknowledgement

References

1. Klimov, V.; Mikhailovsky, A.; Xu, S.; Malko, A.; Hollingsworth, J.; Leatherdale, a. C.; Eisler, H.-J.; Bawendi, M. Optical gain and stimulated emission in nanocrystal quantum dots. *science* **2000**, *290*, 314–317.

2. Bisschop, S.; Geiregat, P.; Aubert, T.; Hens, Z. The impact of core/shell sizes on the optical gain characteristics of CdSe/CdS quantum dots. *ACS nano* **2018**, *12*, 9011–9021.

3. Tanghe, I.; Llusar, J.; Climente, J. I.; Barker, A.; Paternò, G.; Scotognella, F.; Polovitsyn, A.; Khan, A. H.; Hens, Z.; Van Thourhout, D., *et al.* Role of Thermally Occupied Hole States in Room-Temperature Broadband Gain in CdSe/CdS Giant-Shell Nanocrystals. *Advanced Optical Materials* **2022**, *10*, 2201378.

4. Geiregat, P.; Tomar, R.; Chen, K.; Singh, S.; Hodgkiss, J. M.; Hens, Z. Thermodynamic equilibrium between excitons and excitonic molecules dictates optical gain in colloidal cdse quantum wells. *The Journal of Physical Chemistry Letters* **2019**, *10*, 3637–3644.

5. Ahn, N.; Livache, C.; Pinchetti, V.; Jung, H.; Jin, H.; Hahm, D.; Park, Y.-S.; Klimov, V. I. Electrically driven amplified spontaneous emission from colloidal quantum dots. *Nature* **2023**, *617*, 79–85.

6. Geuchies, J. J.; Brynjarsson, B.; Grimaldi, G.; Gudjonsdottir, S.; Van Der Stam, W.; Evers, W. H.; Houtepen, A. J. Quantitative electrochemical control over optical gain in quantum-dot solids. *ACS nano* **2020**, *15*, 377–386.

7. Geuchies, J. J.; Dijkhuizen, R.; Koel, M.; Grimaldi, G.; Du Fossé, I.; Evers, W. H.; Hens, Z.; Houtepen, A. J. Zero-threshold optical gain in electrochemically doped nanoplatelets and the physics behind it. *ACS nano* **2022**, *16*, 18777–18788.

8. Geiregat, P.; Houtepen, A. J.; Sagar, L. K.; Infante, I.; Zapata, F.; Grigel, V.; Allan, G.; Delerue, C.; Van Thourhout, D.; Hens, Z. Continuous-wave infrared optical gain and amplified spontaneous emission at ultralow threshold by colloidal HgTe quantum dots. *Nature Materials* **2018**, *17*, 35–42.

9. Van Avermaet, H.; Schiettecatte, P.; Hinz, S.; Giordano, L.; Ferrari, F.; Nayral, C.; Delpech, F.; Maultzsch, J.; Lange, H.; Hens, Z. Full-spectrum InP-based quantum dots with near-unity photoluminescence quantum efficiency. *ACS nano* **2022**, *16*, 9701–9712.

10. Klimov, V. I.; Ivanov, S. a.; Nanda, J.; Achermann, M.; Bezel, I.; McGuire, J. a.; Piryatinski, A. Single-exciton optical gain in semiconductor nanocrystals. *Nature* **2007**, *447*, 441–6.

11. Wu, K.; Park, Y.-S.; Lim, J.; Klimov, V. I. Towards zero-threshold optical gain using charged semiconductor quantum dots. *Nature Nanotechnology* **2017**, *12*, 1140–1147.

12. Geiregat, P.; Houtepen, A. J.; Sagar, L. K.; Infante, I.; Zapata, F.; Grigel, V.; Allan, G.; Delerue, C.; Van Thourhout, D.; Hens, Z. Continuous-wave infrared optical gain and amplified spontaneous emission at ultralow threshold by colloidal HgTe quantum dots. *Nature Materials* **2017**, *17*, 35–42.

13. Cassidy, J.; Diroll, B. T.; Mondal, N.; Berkinsky, D. B.; Zhao, K.; Harankahage, D.; Porotnikov, D.; Gately, R.; Khon, D.; Proppe, A.; Bawendi, M. G.; Schaller, R. D.; Malko, A. V.; Zamkov, M. Quantum Shells Boost the Optical Gain of Lasing Media. *ACS Nano* **2022**, *16*, 3017–3026.

14. Ithurria, S.; Tessier, M. D.; Mahler, B.; Lobo, R. P. S. M.; Dubertret, B.; Efros, A. L. Colloidal nanoplatelets with two-dimensional electronic structure. *Nature Materials* **2011**, *10*, 936–941.

15. Guzelturk, B.; Pelton, M.; Olutas, M.; Demir, H. V. Giant Modal Gain Coefficients in Colloidal II-VI Nanoplatelets. *Nano Letters* **2018**, *19*, 277–282.

16. Li, Q.; Liu, Q.; Schaller, R. D.; Lian, T. Reducing the Optical Gain Threshold in Two-Dimensional CdSe Nanoplatelets by the Giant Oscillator Strength Transition Effect. *J. Phys. Chem. Lett.* **2019**, *10*, 1624–1632.

17. Tanghe, I.; Samoli, M.; Wagner, I.; Cayan, S. A.; Khan, A. H.; Chen, K.; Hodgkiss, J.; Moreels, I.; Thourhout, D. V.; Hens, Z., *et al.* Optical gain and lasing from bulk cadmium sulfide nanocrystals through bandgap renormalization. *Nature Nanotechnology* **2023**, 1–7.

18. Harankahage, D.; Cassidy, J.; Beavon, J.; Huang, J.; Brown, N.; Berkinsky, D. B.; Marder, A.; Kayira, B.; Montemurri, M.; Anzenbacher, P., *et al.* Quantum Shell in a Shell: Engineering Colloidal Nanocrystals for a High-Intensity Excitation Regime. *Journal of the American Chemical Society* **2023**,

19. Xie, W.; Stöferle, T.; Raino, G.; Aubert, T.; Bisschop, S.; Zhu, Y.; Mahrt, R. F.; Geiregat, P.; Brainis, E.; Hens, Z., *et al.* On-Chip Integrated Quantum-Dot–Silicon-Nitride Microdisk Lasers. *Advanced Materials* **2017**, *29*, 1604866.

20. Akahane, Y.; Asano, T.; Song, B.-S.; Noda, S. High-Q photonic nanocavity in a two-dimensional photonic crystal. *nature* **2003**, *425*, 944–947.

21. Yoshida, M.; Katsuno, S.; Inoue, T.; Gelleta, J.; Izumi, K.; De Zoysa, M.; Ishizaki, K.; Noda, S. High-brightness scalable continuous-wave single-mode photonic-crystal laser. *Nature* **2023**, 1–6.

22. Adachi, M. M.; Fan, F.; Sellan, D. P.; Hoogland, S.; Voznyy, O.; Houtepen, A. J.; Parrish, K. D.; Kanjanaboos, P.; Malen, J. A.; Sargent, E. H. Microsecond-sustained lasing from colloidal quantum dot solids. *Nature communications* **2015**, *6*, 8694.

23. Fan, F.; Voznyy, O.; Sabatini, R. P.; Bicanic, K. T.; Adachi, M. M.; McBride, J. R.; Reid, K. R.; Park, Y.-S.; Li, X.; Jain, A., *et al.* Continuous-wave lasing in colloidal quantum dot solids enabled by facet-selective epitaxy. *Nature* **2017**, *544*, 75–79.

24. Inoue, T.; Yoshida, M.; Zoysa, M.; Ishizaki, K.; Noda, S. Design of photonic-crystal surface-emitting lasers with enhanced in-plane optical feedback for high-speed operation. *Optics Express* **2020**, *28*, 5050–5057.

25. Yokoyama, M.; Noda, S. Finite-difference time-domain simulation of two-dimensional photonic crystal surface-emitting laser. *Optics Express* **2005**, *13*, 2869–2880.

26. Sakai, K.; Miyai, E.; Sakaguchi, T.; Ohnishi, D.; Okano, T.; Noda, S. Lasing band-edge identification for a surface-emitting photonic crystal laser. *IEEE Journal on Selected Areas in Communications* **2005**, *23*, 1335–1340.

27. Wang, Z.; Wang, P.; Lu, H.; Meng, B.; Wang, Y.; Tong, C.; Wang, L. Symmetry criterion and far-field control of photonic-crystal surface-emitting lasers. *Applied Sciences* **2022**, *12*, 10581.

28. Riechel, S.; Kallinger, C.; Lemmer, U.; Feldmann, J.; Gombert, A.; Wittwer, V.; Scherf, U. A nearly diffraction limited surface emitting conjugated polymer laser utilizing a two-dimensional photonic band structure. *Applied Physics Letters* **2000**, *77*, 2310–2312.

29. Ahn, N.; Park, Y.-S.; Livache, C.; Du, J.; Gungor, K.; Kim, J.; Klimov, V. I. Optically Excited Lasing in a Cavity-Based, High-Current-Density Quantum Dot Electroluminescent Device. *Advanced Materials* **2023**, *35*, 2206613.

30. Chen, K.; Gallaher, J. K.; Barker, A. J.; Hodgkiss, J. M. Transient grating photoluminescence spectroscopy: An ultrafast method of gating broadband spectra. *Journal of Physical Chemistry Letters* **2014**, *5*, 1732–1737.